ACS APPLIED NANO MATERIALS

www.acsanm.org Article

# Protein-Templated Core/Shell Au Nanostructures for Intracellular Reactive Oxygen Species Detection by SERS

Muzahidul I. Anik,[§] Animesh Pan,[§] Md Golam Jakaria, Samantha A. Meenach, and Geoffrey D. Bothun*

Cite This: *ACS Appl. Nano Mater.* 2022, 5, 14356−14366 Read Online

ACCESS | Metrics & More | Article Recommendations | Supporting Information

**ABSTRACT:** Core/shell gold "raspberry" nanostructures capable of multiple therapeutic functionalities were synthesized using a template composed of monodispersed anionic protein (bovine serum albumin) nanoparticles coated with a cationic biopolymer (poly-L-lysine). The nanostructures exhibited high photothermal conversion efficiency when exposed to a near-infrared (NIR) laser, which led to significant cellular inhibition of A549 human lung cancer cells due to intracellular hyperthermia. The raspberry structures also provided hot spots for surface-enhanced Raman scattering (SERS) ratiometric sensing of intracellular reactive oxygen species (ROS) when modified with the Raman reporter molecule 4-aminothiophenol (4-ATP). ROS was detected in A549 lung cancer cells upon photothermal heating of internalized nanostructures, enabling a possible mechanism for feedback on therapeutic efficacy. This was confirmed by adding the antioxidant *N*-acetylcysteine (NAC) and using a complementary fluorescence technique, which showed that the amount of detectable intracellular ROS decreased. These safe-by-design gold raspberry nanostructures could be promising for simultaneous therapeutic applications and monitoring therapeutic efficacy.

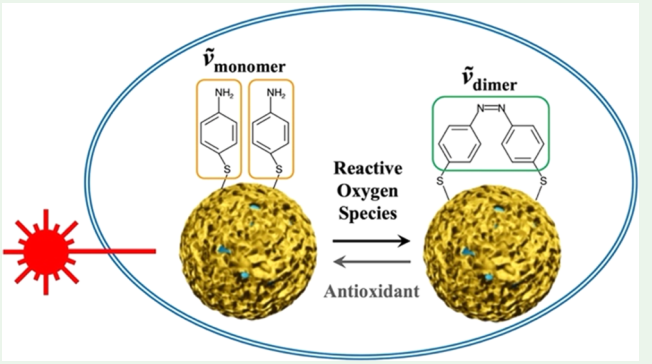


**KEYWORDS:** *core/shell nanoparticle, gold nanostructure, reactive oxygen species, surface-enhanced Raman scattering, hyperthermia, lung cancer cells*



## INTRODUCTION

Near-infrared (NIR) responsive photothermal therapy (PTT) is viewed as a minimally invasive and efficient treatment approach for tumor management.[1−3] Extensive studies on PTT have been conducted using different types of materials, including metal nanomaterials (gold, platinum),[4,5] carbon-based nanomaterials,[6,7] semiconductor nanomaterials (copper),[8] and conducting polymers.[9,10] Gold-based plasmonic nanomaterials have received the most attention for PTT because of their tunable physical and optical properties.[11] Gold nanorods,[12,13] nanocages,[14,15] nanoshells,[16−19] nanostars,[20,21] and nanorods[22,23] are reported to be effective PTT agents that minimize the potential for undesirable side effects.[12,15,24]

Cellular inhibition caused by PTT is a result of intracellular heating that can lead to the formation of reactive oxygen species (ROS).[25,26] ROS are highly reactive chemical species that play important roles in modulating cell signaling, differentiation, and death as well as tissue inflammation.[27] Cancer cells exhibit higher metabolic oxidative stress compared with normal cells, which is mostly due to intrinsic dysfunction of mitochondria and activation of nicotinamide adenine dinucleotide phosphate (NADPH) oxidases.[28,29] ROS generation caused by nanoparticles (NPs) initiates a sequence of pathological events governed by the composition and physicochemical features of NPs such as size, charge, and surface chemistry.[26,30] Detecting ROS generation in cells exposed to nanomaterials is important to determine mechanisms of toxicity and therapeutic action. Fluorescence is commonly used for measuring intracellular ROS[31] but is limited due to photobleaching of probe molecules or quenching in the presence of metallic nanostructures such as gold.[32,33]

Surface-enhanced Raman scattering (SERS) is a sensitive, noninvasive tool for molecular detection and in biological environments.[34] SERS "nanoprobes" have been used to examine interactions between nanomaterials and intracellular environments and to map the cellular distribution in both live cells and fixed cells, providing an interesting platform for multimode imaging and detection.[35,36] The few studies conducted on SERS-based ROS detection in cellular environments have demonstrated the promise of this novel

**Received:** June 16, 2022
**Accepted:** September 14, 2022
**Published:** September 28, 2022

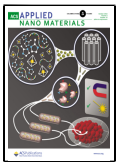




https://doi.org/10.1021/acsanm.2c02641
*ACS Appl. Nano Mater.* 2022, 5, 14356−14366

Scheme 1. Protein-Templated Gold Raspberry Nanostructures[a46]

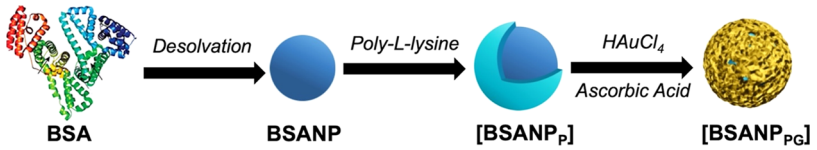


[a]Bovine serum albumin nanoparticles [BSANP] are formed by desolvation, coated with poly-L-lysine[$BSANP_P$], and template the synthesis of goldnanoshells [$BSANP_{PG}$]. [$BSANP_{PG}$] are then surface-functionalized with a Raman reporter molecule 4-aminothiophenol, 4-ATP-[$BSANP_{PG}$]. The BSA protein structure was used with permission,[46] Copyright (2019) American Chemical Society.

approach.[37−40] The general strategy involves intracellular ROS-induced chemical reactions of Raman reporter molecules detected by nanostructures designed with SERS "hot spots."[37,38,41]

Motivated by this prior work, we have examined the potential to simultaneously achieve PTT and detect the resulting ROS that is generated by core/shell "gold raspberry nanostructures" formed using biopolymer-coated bovine serum albumin (BSA) nanoparticles [BSANP] as templates (Scheme 1). Protein-based nanoparticles may be excellent biocompatible candidates for creating gold nanostructures; for example, serum albumin is an effective carrier of therapeutic drugs and imaging agents.[42−45] The intermediate layer coating the protein nanoparticle template, an adsorbed cationic biopolyelectrolyte, enriches the surface with gold anions that are then reduced to form gold raspberry nanoshells. In addition to being less dense and less prone to long-term sedimentation, self-assembled "soft-templated" nanostructures provide further advantages over the "hard-templates" because they can adopt unique shapes, respond to the fabrication process, and accommodate additional cargos. By functionalizing the surface with the Raman reporter 4-aminothiophenol (4-ATP), we demonstrate a multifunctional platform for PTT and intracellular ROS detection using a model cancer cell line, A549 human lung adenocarcinoma epithelial cells.

## EXPERIMENTAL SECTION

**Materials and Methods.** BSA (66 kDa), poly-L-lysine (15−30 kDa), glutaraldehyde (8%), chloroauric acid ($HAuCl_4{\cdot}3H_2O$), *N*-acetylcysteine (NAC), hydrogen peroxide ($H_2O_2$), and copper sulfate ($CuSO_4$) were purchased from Sigma-Aldrich (St. Louis). Sodium chloride (NaCl), ascorbic acid (AA), and 4-aminothophenol (4-ATP) were obtained from Thermo Fisher Scientific. All materials were used as received. A Millipore water system (Direct 3Q @ UV) provided high-purity water used for all experiments. A549 human lung adenocarcinoma epithelial cells were obtained from American Type Culture Collection (ATCC, Manassas, VA). 3-(4,5-Dimethylthiazol-2-yl)-2,5-diphenyltetrazolium bromide (MTT) was purchased from Invitrogen, and fetal bovine serum (FBS) was obtained from Atlanta Biologics (Flowery Branch, GA). Dulbecco's modified Eagle's medium (DMEM, 4.5 g $L^{-1}$ D-glucose and L-glutamine) and trypsin-EDTA (0.25%) were obtained from Life Technologies (Carlsbad, CA). Sodium pyruvate, penicillin-streptomycin, and fungizone were obtained from GE Health Life Sciences (Pittsburgh, PA).

**Preparation of Poly-L-lysine-Coated BSA Nanoparticles ([$BSANP_P$]).** [BSANP] were prepared using a modified desolvation method. A 10 mg $mL^{-1}$ BSA solution (2 mL) was prepared at pH 7.4 (10 mM NaCl) and stirred for 30 min. Ethanol was added dropwise to a final volume of 10 mL. To this turbid solution, 25 $\mu$L of 5% glutaraldehyde was added, and the nanoparticle suspension was stirred for 20 h to yield cross-linked [BSANP]. The nanoparticles were washed three times with water by centrifuging at 12,000 rpm for 10 min, redispersed in 10 mL Millipore water, and stored at 4 °C for further use. [BSANP] were coated with poly-L-lysine (PLL) by adding them dropwise to 0.5 mg $mL^{-1}$ (3 mL) of PLL in water under magnetic stirring for 15 min and incubating for 1 h at room temperature. [$BSANP_P$] were centrifuged three times at 5000 rpm for 7 min to remove the excess PLL from the solution. The samples were resuspended in 7 mL of deionized water and stored at 4 °C until further use.

**Preparation of 4-ATP-[$BSANP_{PG}$].** [$BSANP_{PG}$] were prepared by direct reduction of $HAuCl_4$ to yield Au nanoparticles using ascorbic acid (AA). $HAuCl_4$ dissolved in water was added to [$BSANP_P$] at a ratio of 5 mM $HAuCl_4{\cdot}3H_2O$ to 1.43 mg BSA $mL^{-1}$ ($1.4 \times 10^{-3}$ mass ratio) to allow the $AuCl_4^-$ to electrostatically bind to the PLL coating. AA was then added at an AA/$AuCl_4^-$ molar ratio of 2 to form Au nanoparticles, upon which the translucent white color of the suspensions abruptly changed to blue, indicative of gold nanoshells forming on the [$BSANP_P$] surfaces. [$BSANP_{PG}$] were labeled with Raman reporter molecule 4-ATP by incubating 3 mL of [$BSANP_{PG}$] solution with 20 mM of 4-ATP. The resulting solutions were kept for 15 min under stirring condition at room temperature until the system reached equilibrium based on visual observation of the color change. 4-ATP-[$BSANP_{PG}$] were washed three times by centrifugation at 1000 g for 10 min and dispersing in water.

**Nanostructure Characterization.** The z-averaged hydrodynamic diameter ($D_h$) and zeta potential ($\zeta$) were measured using a Malvern Zetasizer Nano ZS (Worcestershire, U.K.) equipped with a back-scattering detector angle of 173° and a 4 mW, 633 nm He−Ne laser. $\zeta$ was determined by combined Doppler electrophoretic velocimetry and phase analysis light scattering using folded capillary cells. Three parallel measurements were taken for all samples. [BSANP], [$BSANP_P$], and 4-ATP-[$BSANP_{PG}$] nanostructures were analyzed by transmission electron microscopy (TEM, JEOL JEM-2100F) operating at 200 kV. For TEM, 5 $\mu$L of samples were spread and slowly dried onto a carbon-coated copper grid with 300 mesh. [BSANP], [$BSANP_P$], and 4-ATP-[$BSANP_{PG}$] nanostructures were also analyzed by SEM equipped with a field emission gun (Zeiss Sigma VP FE-SEM) at an operating voltage of 5 kV. A 10 $\mu$L of sample suspension was drop-cast on a silicon wafer and dried under vacuum conditions overnight. Since [BSANP] and [$BSANP_P$] nanoparticles are nonconductive in nature, they sputter-coated with gold (Cressington 108 auto gold coater). Elemental maps were generated using energy-dispersive X-ray spectroscopy (EDS, Oxford Inca). Absorption spectra were recorded using an Ultraviolet−visible/near-infrared (UV−vis/NIR) scanning spectrophotometer (JASCO V-780) and circular dichroism spectra using a circular dichroism spectropolarimeter (Jasco J-1100) at 25 °C.

**Surface Plasmon Simulation.** The electric field of [$BSANP_{PG}$] was simulated (FDTD solutions, Lumerical Inc.) using a TEM image of a [$BSANP_{PG}$] cluster. The boundaries were set as perfectly matched layers (PMLs) in the *x*, *y*, and *z* directions of the simulation boundaries. The dielectric constant was set to 1 for vacuum. The temperature of the simulation was 25 °C, and the simulation time was 1000 fs. A total-field scatter-field source was used to pulse the nanostructure system with 785 nm laser, which was recorded using scattered field monitors. The excitation light was in the *z*-direction, perpendicular to the imaging plane. A mesh size of 2 $nm^3$ and refractive index and excitation coefficient of gold were used based on Johnson and Christy in the simulation. The maximum electric field, $E_{max}$, was determined by monitoring the scattered field monitor.



https://doi.org/10.1021/acsanm.2c02641
ACS Appl. Nano Mater. 2022, 5, 14356−14366

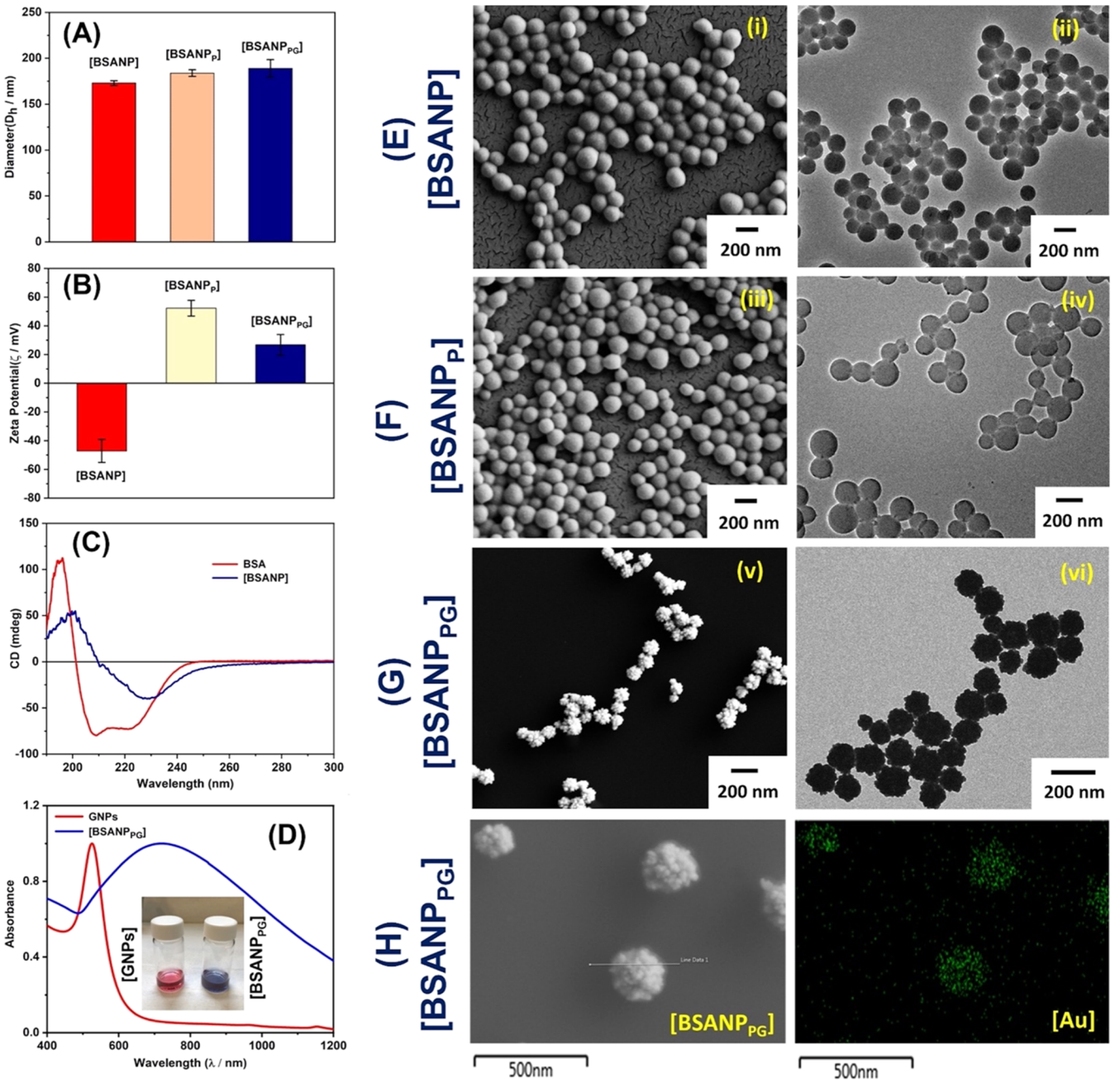


**Figure 1.** Nanostructure characterization. (A) Hydrodynamic diameter ($D_h$) and (B) zeta potential ($\zeta$) of [BSANP], [BSANP$_P$], and [BSANP$_{PG}$]; (C) circular dichroism spectra of BSA and [BSANP]; and (D) UV−vis spectra of GNPs and [BSANP$_{PG}$] (inset: digital image of particle solutions). All measurements were performed in DI water. Representative FE-SEM (i, iii, v) and TEM (ii, iv, vi) images are shown for (E) [BSANP], (F) [BSANP$_P$], and (G) [BSANP$_{PG}$]. (H) SEM-EDS map shows the particles and their corresponding elemental distribution of gold.

**Photothermal Study of 4-ATP-[BSANP$_{PG}$] Raspberry Nanostructures.** Photothermal heating and conversion efficiency were determined by irradiating 500 $\mu$L of 4-ATP-[BSANP$_{PG}$] in a glass vial using a 730 nm NIR laser (MDL-III-730) for 10 min, with power densities of 1.8 and 2.6 W cm$^{-2}$. Changes in temperature were monitored at 30 s increments using a thermocouple (Pico Technology Ltd.).

The photothermal conversion efficiency ($\eta$) of 4-ATP-[BSANP$_{PG}$] was determined according to reported methods[47,48]

$$\eta = \frac{hS(T_{max} - T_{surr}) - Q_{dis}}{I(1 - 10^{-A_{730}})} \quad (1)$$

where $h$ is the heat transfer coefficient, $S$ is the surface area of the container, $T_{max}$ is the maximum steady-state temperature of the sample solution, $T_{surr}$ is the ambient surrounding temperature, $Q_{dis}$ is the heat dissipated from the light absorbed by the solvent and container, $I$ is the laser power (2.6 W cm$^{-2}$), and $A_{730}$ is the absorbance of the sample solution at 730 nm.

***In Vitro* Cytotoxicity.** MTT assays were conducted to determine the viability of A549 cells exposed to 4-ATP-[BSANP$_{PG}$] with or without laser exposure. Cells were seeded in a 96-well plate at a concentration of 2 × 10$^4$ cells mL$^{-1}$ with DMEM media (containing 1 mM sodium pyruvate, 1% penicillin-streptomycin, and 10% FBS) and allowed to grow at 37 °C overnight in 5% $CO_2$. 4-ATP-[BSANP$_{PG}$] dispersed in DMEM were then added into the wells. After 24 h of incubation, the cells were washed three times with 1× PBS, and 200 $\mu$L of a freshly prepared (5 mg mL$^{-1}$) MTT solution was added with 1 h of incubation at 37 °C in 5% $CO_2$. The culture media were


https://doi.org/10.1021/acsanm.2c02641
ACS Appl. Nano Mater. 2022, 5, 14356−14366

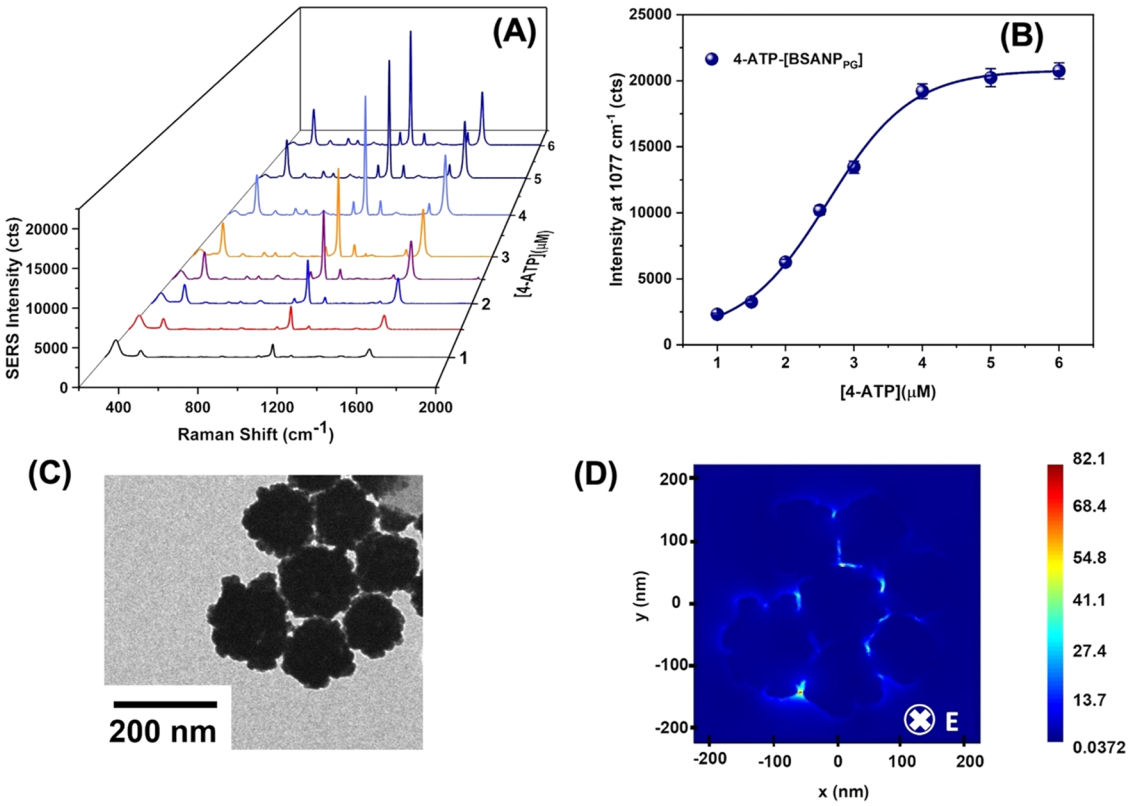


**Figure 2.** SERS study of 4-ATP-[$BSANP_{PG}$] on dispersed gold nanostructures. (A) Raman spectra of 4-ATP on [$BSANP_{PG}$] surface and (B) the intensity at 1077 $cm^{-1}$ as a function of 4-ATP concentration. (C) Representative TEM image used in the (D) surface plasmon simulation of the electric field distribution at 785 nm in the *xy*-plane for [$BSANP_{PG}$].

discarded, 100 $\mu$L of DMSO was added to each well, the samples were shaken for 10 min, and the absorbance was measured at 540 nm using a multiplate reader (Spectra Max M2). For *in vitro* cell culture, A549 cells were seeded and incubated with different concentrations of 4-ATP-[$BSANP_{PG}$] in 96-well plates. After 4 h of incubation, the cells were washed twice with a PBS solution to remove excess 4-ATP-[$BSANP_{PG}$] and replaced with fresh cultured media. The cells were irradiated with a 730 nm laser as a function of time (2, 5, 10 min) and laser power density (1, 1.8, and 2.6 W $cm^{-2}$), after which they were cultured for an additional 24 h. To investigate the effect of antioxidant *N*-acetylcysteine (NAC), the cells were irradiated with a 730 nm laser for 10 min at 2.6 W $cm^{-2}$, after which 2.5 mM NAC was added to the well plates, and the cells were incubated for 1 h. A minimum of three parallel sample sets were performed in each group, and these sets were tested in triplicate. The cell viability (%) was calculated according to the equation cell viability (%) = [OD@540 nm(sample)]/[OD@540 nm(control)] × 100%, where OD is the optical density.

**Intracellular ROS Analysis Using Fluorescence Study.** The dye 2′,7′-dichlorofluorescin diacetate (DCFDA) was used for the detection of 4-ATP- [$BSANP_{PG}$]-induced ROS generation. To investigate the ROS production from cancer cells during PTT, A549 cells were seeded at the density of 20,000 in clear bottom black 96-well plates, and 200 $\mu$L of 150 $\mu$g $mL^{-1}$ 4-ATP-[$BSANP_{PG}$] was added and incubated with the cells for 24 h. The cells were washed with PBS (1× buffer), refilled with fresh media, and irradiated with a 730 nm laser for 10 min. After treatment, the fluorescence intensity (at $\lambda_{ex}$ = 595 nm, $\lambda_{em}$ = 520 nm) was measured after 30 min of DCFDA (5 $\mu$M) addition using a Cytation 3 plate reader (BioTek, Winooski, VT). NAC was added to the NIR laser-treated cells at a concentration of 2.5 mM, and the cells were incubated for 30 min. Four plates were designed using (i) cells, (ii) cells + 4-ATP-[$BSANP_{PG}$], (iii) cells + 4-ATP-[$BSANP_{PG}$] + laser exposure, and (iv) cells + 4-ATP-[$BSANP_{PG}$] + laser exposure + NAC.

**SERS Measurements and Confocal Raman Microscopy.** SERS was measured using a SIERRA 2.0 Raman Spectrometer (Snowy Range Instruments, WY) with a 785 nm laser directed at a power of 100 mW and integration time of 1 s. Measurements were performed over a wavenumber range of 200 to 2000 $cm^{-1}$ using orbital raster scanning. In a typical liquid-state SERS experiment, 2 mL of freshly made 4-ATP-[$BSANP_{PG}$] solution was introduced into a cuvette and measured in triplicate.

Confocal Raman studies were conducted using two methods. For the first, cells were seeded in 35 mm glass bottom microwell dishes (MatTek) at a concentration of 250,000 cells/dish and incubated overnight at 37 °C and 5.0% $CO_2$. The media was removed, replaced with 4-ATP-[$BSANP_{PG}$] diluted media, and incubated for 0.5, 2, 4, and 8 h. Afterward, 4-ATP-[$BSANP_{PG}$] containing media was removed at different time points and washed three times with PBS (1× buffer, Gibco). The samples were fixed using 4% paraformaldehyde in PBS for 10 min, rinsed three times with PBS buffer, and refilled with fresh PBS. The second method was used to investigate ROS generation. Cells were seeded in 8 well chambers with high-performance glass coverslips (Cellvis) at a concentration of 35,000 cells/well and cultured for 24 h. The cells were incubated with 200 $\mu$L of 150 $\mu$g $mL^{-1}$ 4-ATP-[$BSANP_{PG}$] for 4 h, washed with PBS, and irradiated with a 730 nm laser for 10 min. To study the effect of antioxidants on the generated ROS, NAC was added to the wells at 2.5 mM, and the cells were incubated for 30 min. Three plates were designed using (i) cells + 4-ATP-[$BSANP_{PG}$], (ii) cells + 4-ATP-[$BSANP_{PG}$] + NIR laser exposure, and (iii) cells + 4-ATP-[$BSANP_{PG}$] + NIR laser exposure + NAC.

An inverted confocal Raman microscope (Alpha300 R, WiTec, Germany) was used for imaging, equipped with a Nikon CFI-Achro 60x/0.8 air objective, a 785 nm laser source set to 15 mW, and a CCD detector with a 600 lines $mm^{-1}$ grating. Regions of interest were scanned with 0.2 s integration time, 100 points per line, and 100 lines per area (150 × 150 $\mu m^2$) to obtain the Raman spectral data. Each spectrum was averaged over three scans. Global background subtraction and cosmic-ray removal were performed using WiTec Control 5.0 software. Confocal Raman data were acquired for C−S at


https://doi.org/10.1021/acsanm.2c02641
ACS Appl. Nano Mater. 2022, 5, 14356−14366

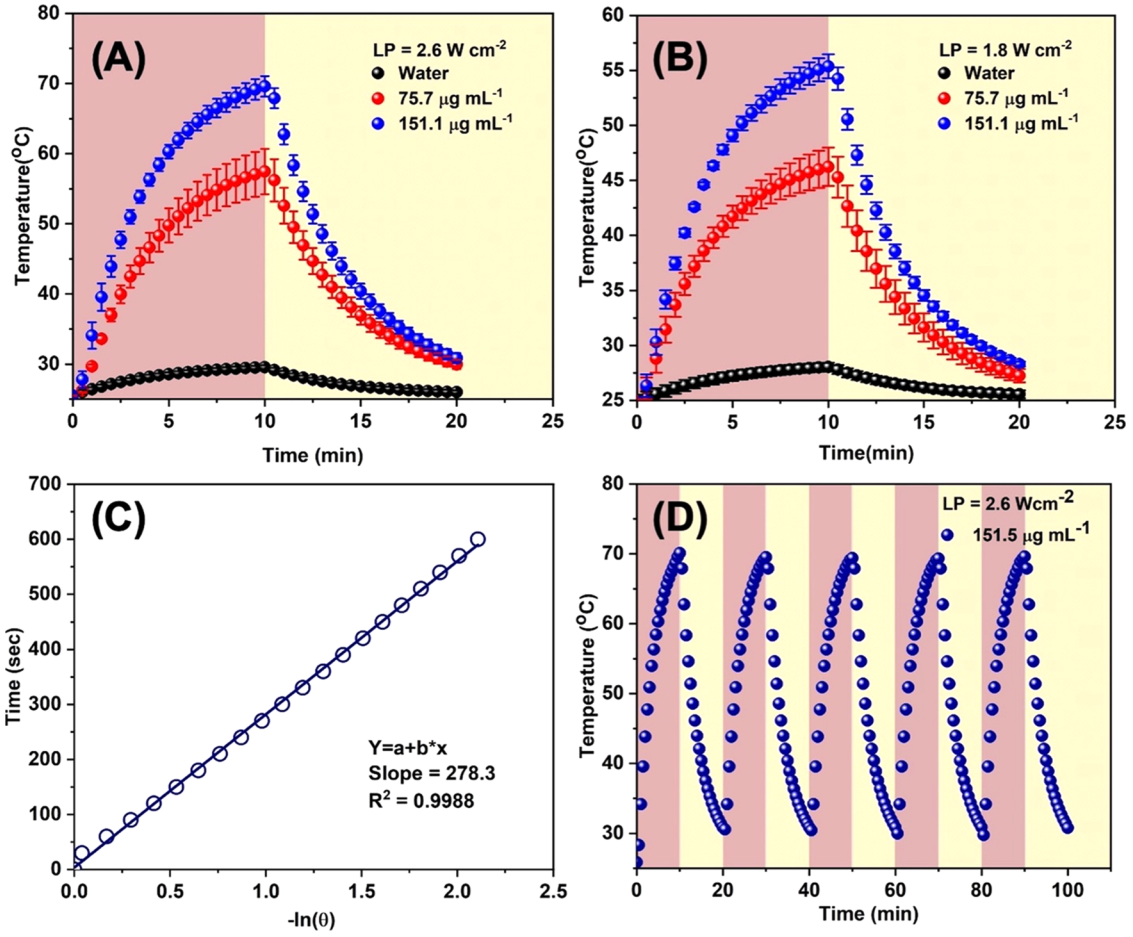


**Figure 3.** Photothermal properties of 4-ATP-[$BSANP_{PG}$]. (A) Temperature change of 4-ATP-[$BSANP_{PG}$] solutions (two different Au concentrations) upon exposure for 10 min using a 730 nm NIR laser at power densities of (A) 2.6 W $cm^{-2}$ and (B) 1.8 W $cm^{-2}$. From heating and cooling, the (C) time *vs* -ln($\theta$) plot was used to calculate photothermal efficiency. (D) Temperature change of 4-ATP-[$BSANP_{PG}$] solutions at maximum power (2.6 W $cm^{-2}$) over 5 on/off laser exposure cycles.

1077 $cm^{-1}$ and C−N at 1142 $cm^{-1}$ (see the Supporting Information for additional details).

**Statistical Analysis.** Experimental results are expressed as the mean ± standard deviation of three independent experiments. Unpaired, two-tailed *t*-tests were used to evaluate significant differences between a pair of groups. Levels of significance were $p < 0.05$ (*), $p < 0.01$ (**), and $p < 0.001$ (***). The statistical analysis was completed using OriginPro 2019 software. Image analysis was performed using ImageJ software.[49]

## RESULTS AND DISCUSSION

**Preparation and Characterization of Nanostructures.** [BSANP] prepared by a modified desolvation method[50−52] were monodispersed with an average hydrodynamic diameter, polydispersity index (PDI), and $\zeta$ of 173 ± 3 nm, 0.06 ± 0.04, and −47 ± 2 mV, respectively (Figure 1A,B,E). The secondary structure of BSA changed from predominantly $\alpha$ helical ($\alpha$) as free protein in solution to $\beta$ sheet ($\beta$) upon [BSANP] formation (Figure 1C), which is consistent with previous work.[53] Upon coating with poly-L-lysine, the particles became cationic and larger but remained monodispersed (Figure 1A,F). The apparent thickness of the poly-L-lysine coating was 5.9 nm based on the hydrodynamic diameter, and the average PDI value was 0.07 ± 0.05. The coating enriched the interface with $AuCl_4^-$, which was reduced using ascorbic acid to yield gold nanostructures with broad absorbance in the NIR region with a maximum at 722 nm (Figure 1D). Owing to strong plasmonic coupling on the surface of the nanostructures, the LSPR peak of [$BSANP_{PG}$] was red-shifted as compared to gold nanoparticles (GNPs). The "raspberry" structure was confirmed by TEM, FE-SEM, and EDS (Figure 1G,H).

**4-ATP Modification and SERS Enhancement.** SERS was used to determine the 4-ATP surface coverage after modification and the corresponding analytical enhancement factor (AEF) of the conjugated 4-ATP-[$BSANP_{PG}$]. The AEF was calculated as AEF = $(I_{SERS} \times N_{NRS})/(I_{NRS} \times N_{SERS})$, where $I_{SERS}$ and $I_{NRS}$ are the average intensities of the C−S bond stretching from SERS and NRS spectra at 1077 $cm^{-1}$, respectively, and $N_{SERS}$ and $N_{NRS}$ are the number of molecules in the laser probe volume during SERS and NRS measurements. Since the experiments were carried out using the same laser probe volume, $N_{SERS}$ and $N_{NRS}$ can be substituted by the 4-ATP concentration present during the SERS and NRS experiments. The SERS signal increased with increasing 4-ATP concentration up to 4 $\mu$M, where it began to plateau until reaching a 6 $\mu$M concentration which represents complete surface coverage (Figure 2B). From $n = 10$ measurements for each solution, an average AEF equal to $1.81 \times 10^4$ was determined in agreement with previous SERS studies of 4-ATP on gold.[54] The surface plasmon simulation suggests that a strong electromagnetic field was localized and confined in the nanogap of [$BSANP_{PG}$] nanoclusters creating hot spots for the


https://doi.org/10.1021/acsanm.2c02641
ACS Appl. Nano Mater. 2022, 5, 14356−14366

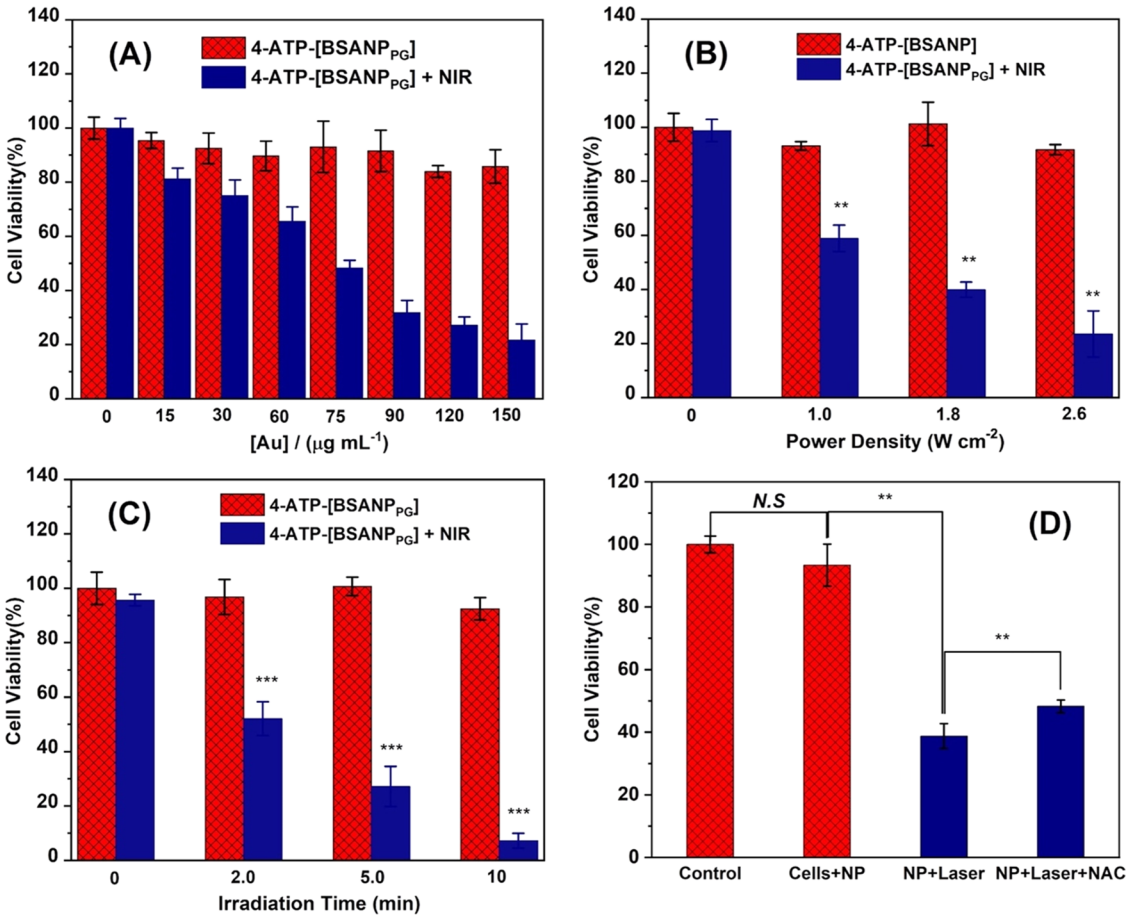


**Figure 4.** *In vitro* A549 cell viability determined by the MTT assay and live/dead cell staining. (A) Viability as a function of (A) 4-ATP-[BSANP$_{PG}$] concentration with and without NIR laser exposure at a power density of 2.6 W cm$^{-2}$, (B) laser power density at 150 μg mL$^{-1}$ 4-ATP-[BSANP$_{PG}$]. Laser exposure was 5 min for (A) and (B). (C) Viability with 4-ATP-[BSANP$_{PG}$] as a function of time with and without laser exposure at 150 μg mL$^{-1}$ 4-ATP-[BSANP$_{PG}$] and a power density of 2.6 W cm$^{-2}$. (D) Viability in the absence (Control) or presence (Cells + NP) of 150 μg mL$^{-1}$ 4-ATP-[BSANP$_{PG}$] with laser exposure (NP + Laser) followed by the addition of 2.5 mM NAC (NP + Laser + NAC).

Raman reporter 4-ATP. The max $[E_{max}/E_0]^4$ was found to be 82.1, which decreased with increased spacing within the nanoclusters (Figure 2D). The max $[E_{max}/E_0]^4$ values are comparable with previous reported values using Au-based nanoplatforms.[55]

After 4-ATP modification, the average hydrodynamic diameter of 4-ATP-[BSANP$_{PG}$] was 193 ± 8 nm, and the ζ was 29 ± 5 mV. The ζ reflects the cationic charge imparted by the 4-ATP ligands. The hydrodynamic diameter and absorbance spectra (results not shown) were nearly identical to that of [BSANP$_{PG}$] (Figure 1A), indicating that the particles remained stable after surface modification. Furthermore, the absorbance spectra in water (Figure 1D) and PBS buffer were similar, with the same maximum absorbance wavelength, indicating that the particles resisted aggregation due to charge screening.

**Photothermal Properties of 4-ATP-[BSANP$_{PG}$].** As shown in Figure 3A,B, the photothermal heating of solutions containing 4-ATP-[BSANP$_{PG}$] was dependent upon concentration and laser power. After 10 min of laser exposure at 2.6 W cm$^{-2}$, the temperature of 4-ATP-[BSANP$_{PG}$] ([Au] = 151.5 μg mL$^{-1}$) increased from room temperature to 69.6 °C ($\Delta T$ = 44.5 °C, Figure 3A). Temperatures in the range of 41 to 47 °C can lead to cell death by hyperthermia.[56] Comparatively, only a slight temperature change ($\Delta T$ = 4.7 °C) was observed for deionized water without the presence of 4-ATP-[BSANP$_{PG}$]. The photothermal conversion efficiency was 44.6% based on the heating and cooling curves of the nanostructures (Figure 3C), which is higher than other gold nanoparticles such as hexapods[57] and nanocages.[58] The electromagnetic hot spots generated on the surface of 4-ATP-[BSANP$_{PG}$] by plasmonic resonance account for the high light-to-heat conversion efficiency. The photothermal stability of 4-ATP-[BSANP$_{PG}$] was evaluated by five laser on/off cycles, where no significant temperature variation was noticed (Figure 3D). There was also minimal change in the Raman signal of the 4-ATP-[BSANP$_{PG}$] during these heating cycles (Figures S1 and S2). The observed photothermal stability indicates that these gold nanostructures were not damaged during multiple heating cycles, maintaining their optical properties for combined intracellular PTT and ROS detection.

***In Vitro* Cytotoxicity and Combined Photothermal Therapy.** Encouraged by the photothermal performance of 4-ATP-[BSANP$_{PG}$], *in vitro* PTT was performed in A549 cells. Figure 4A shows the cell viability of A549 cancer cells after 24 h incubation with different concentrations of 4-ATP-[BSANP$_{PG}$]. Without NIR laser heating, only a small decrease in cell viability was observed in the presence of 4-ATP-[BSANP$_{PG}$], presumably due to the cationic charge presented by these nanostructures. With NIR laser heating, laser exposure


https://doi.org/10.1021/acsanm.2c02641
ACS Appl. Nano Mater. 2022, 5, 14356−14366

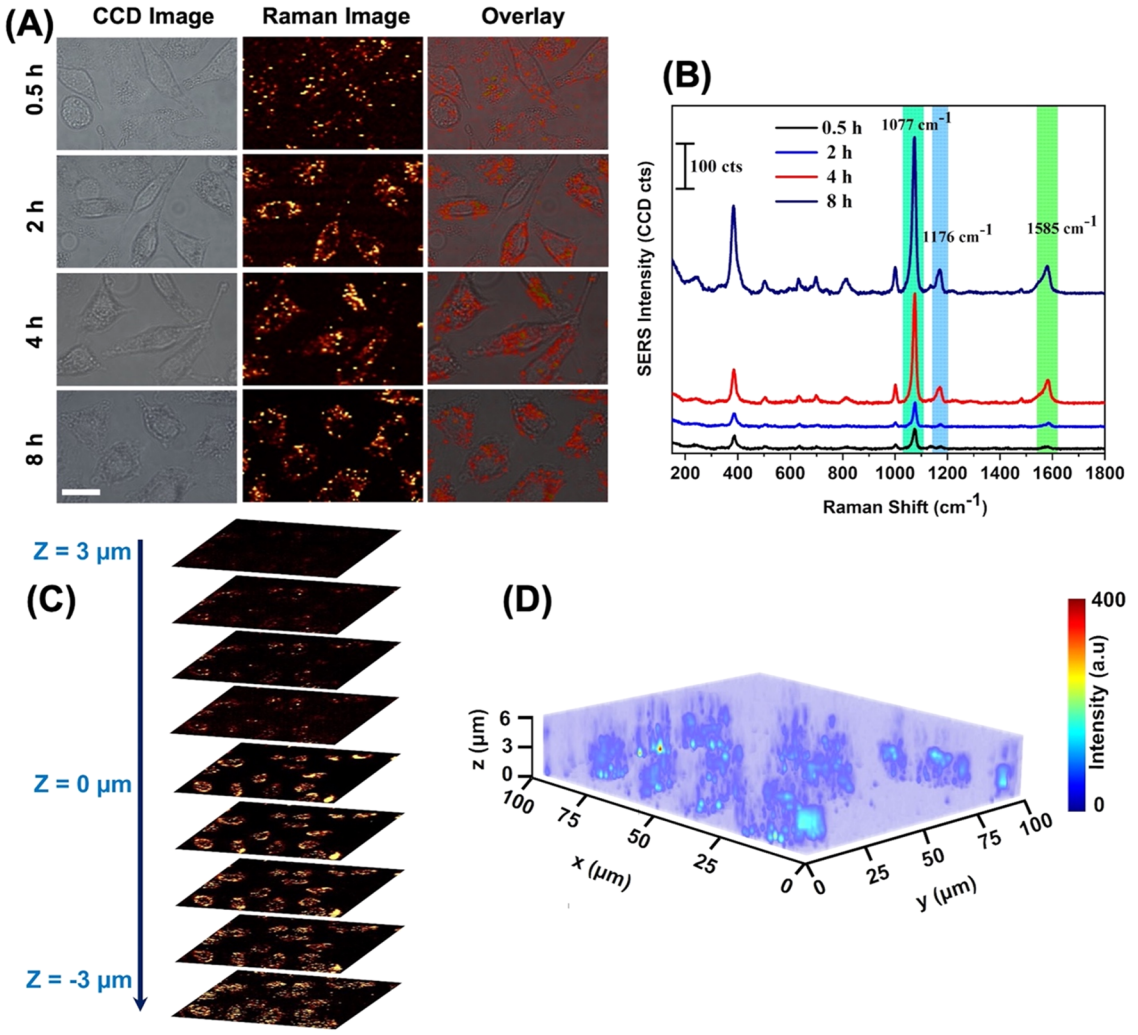


**Figure 5.** (A) Bright-field, Raman, and overlaid images of A549 cells incubated with 4-ATP-[$BSANP_{PG}$] as a function of time (0.5, 2, 4, and 8 h; scale bar = 20 $\mu$m) with the (B) corresponding SERS spectra (base line-corrected) collected from regions where nanostructures were observed. (C) *Z*-stack image sections for SERS imaging of 4-ATP-[$BSANP_{PG}$] at 4 h incubation with A549 cells (the orthogonal *Z*-stack images were collected at $Z = -3, -2, -1, -0.5, 0, 0.5, 1, 2, 3$ $\mu$m). (D) 3D reconstructed Confocal Raman volumetric mapping of 4-ATP-[$BSANP_{PG}$] in cells.

alone did not reduce cell viability, and a dose-dependent reduction in cell viability was observed with increasing concentrations of 4-ATP-[$BSANP_{PG}$]. Cell viability decreased significantly to 58.8, 39.9, and 23.5% with increasing power densities of 1.0, 1.8, and 2.6 W $cm^{-2}$, respectively (Figure 4B), and with increasing exposure times (Figure 4C). The lowest cell viability, 7.2%, was observed when the cells were exposed for 10 min at 2.6 W $cm^{-2}$. The antioxidant NAC was able to partially reduce the negative effects of 4-ATP-[$BSANP_{PG}$] and NIR laser irradiation on A549 cell viability, indicating that NAC scavenged free radical ROS produced due to PTT.

**SERS-Traced Cellular Uptake.** The time-dependent uptake of 4-ATP-[$BSANP_{PG}$] was examined in A549 cells using Raman microscopy enabled by SERS at 0.5, 2, 4, and 8 h. Figure 5A shows the bright-field, Raman, and overlay images. At 0.5 h, the SERS signal was weak, and the nanostructures appear outside of the cells, approaching the cell membrane. 4-ATP-[$BSANP_{PG}$] were internalized over time and concentrated in the cytoplasm, resulting in a stronger SERS signal that was observed over a large area of the cell (using a large area scan). As shown in Figure 5B, 4-ATP-[$BSANP_{PG}$] exhibited SERS bands of the 4-ATP molecules[59] with a linear increase in intensity over time (Figure S3). Cellular uptake of 4-ATP-[$BSANP_{PG}$] was further confirmed using *Z*-stack image analysis and three-dimensional (3D) image reconstruction (Figure 5C,D).

***In Situ* and *In Vitro* SERS-Assisted ROS Detection.** 4-ATP has been reported to dimerize due to radical oxidative coupling, forming 4,4′-dimercaptoazobenzene (DMAB) through a diazonium between adjacent 4-ATP[37] that can be detected and differentiated from 4-ATP using SERS (Figure 6A).[39] We first examined *in situ* ROS detection 4-ATP-[$BSANP_{PG}$] via DMAB formation using superoxide free radicals ($O_2^{\bullet-}$) generated from hydrogen peroxide in the presence of a $Cu^{2+}$ catalyst.[60] Characteristic peaks for 4-ATP at 1077, 1175, and 1585 $cm^{-1}$ are assigned to the $a_1$ symmetry of the vibrational mode (Figure 6B, top blue line).[61] After interacting with ROS, the spectra exhibited three new peaks at 1142, 1386, and 1428 $cm^{-1}$ (Figure 6B, bottom red line) assigned to the $b_2$ symmetry of the vibrational mode.

With DMAB formation due to ROS confirmed *in situ*, we then measured the presence of ROS within A549 cells *in vitro* without NIR laser exposure. After 4 h of internalization (Figure 6C), SERS spectra representing 4-ATP and DMAB were


https://doi.org/10.1021/acsanm.2c02641
ACS Appl. Nano Mater. 2022, 5, 14356−14366

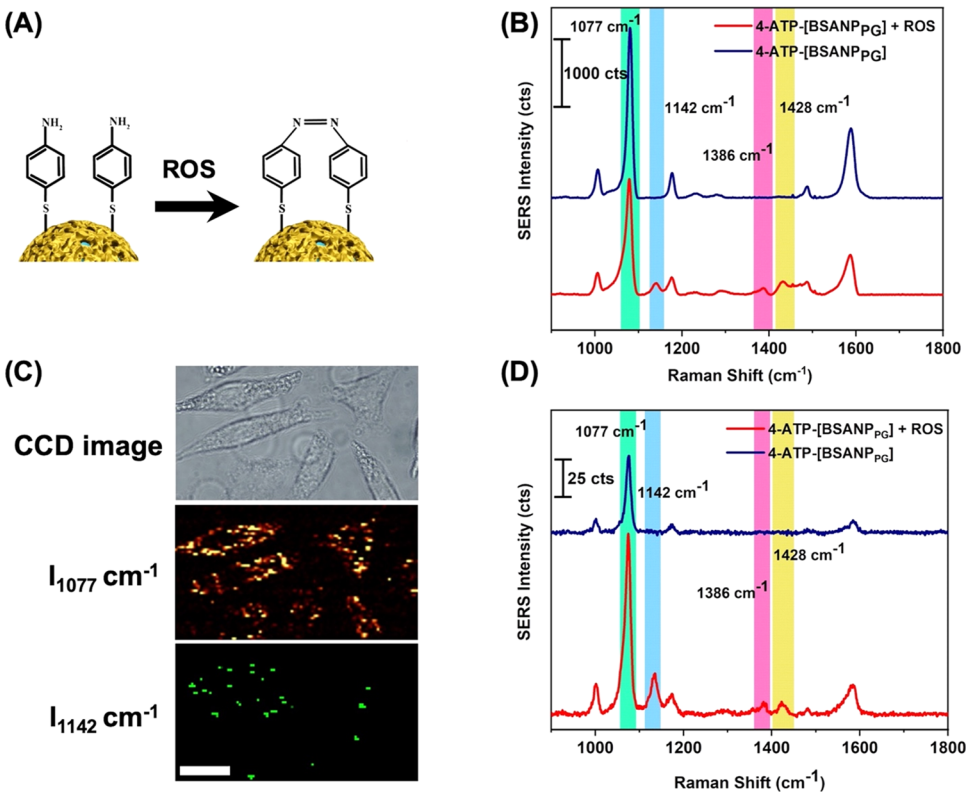


**Figure 6.** (A) Schematic depicting the conversion of 4-ATP to DMAB in the presence of ROS. (B) Raman spectra of 4-ATP-[$BSANP_{PG}$] in solution in the absence (top blue line) and presence (bottom red line) of $O_2^{\bullet-}$ generated *in situ*. (C) Bright-field and Raman image mapping depicting the $I_{1077}$ $cm^{-1}$ (4-ATP) and $I_{1142}$ $cm^{-1}$ (DMAB) of A549 cells incubated with 4-ATP-[$BSANP_{PG}$] for 4 h (scale bar = 20 $\mu$m). (D) Raman spectra obtained from (C) showing the presence of 4-ATP and DMAB ligands within the cytoplasm of A549 cells.

observed with the same characteristic peaks measured *in situ* (Figure 6D). In this case, DMAB was formed by intracellular ROS within the cytoplasm of the A549 cancer cells. While the type of ROS could not be determined from this analysis, Cui et al.[37] have shown that gold nanoparticles functionalized with 4-ATP form DMAB in the presence of $O_2^{\bullet-}$, hydroxyl radicals ($^{\bullet}OH$), peroxyl radicals ($ROO^{\bullet}$), and singlet oxygen ($^1O_2$).

**ROS Sensing in Response to PTT.** Intracellular ROS detection in response to PTT was investigated after the cells were incubated with 4-ATP-[$BSANP_{PG}$] for 4 h and then treated for 10 min with NIR laser exposure. To normalize differences in cell and 4-ATP-[$BSANP_{PG}$] concentrations within the microscopy area scans (Figure 7A) and spectra collected,[37] the ratio of $I_{1142}$ $cm^{-1}$ (4-ATP) and $I_{1077}$ $cm^{-1}$ (DMAB) was used as a proxy for ROS levels (Figure 7B). ROS detected without NIR laser treatment is likely a combination of the cellular basal level and the response to 4-ATP-[$BSANP_{PG}$] exposure. With NIR laser exposure, $I_{1142}/I_{1077}$ increased more than 2-fold ($p < 0.01$) compared to the control group due to ROS-induced DMAB formation (Figure 7B). The ratio $I_{1142}/I_{1077}$ did not change with NIR laser exposure alone in the absence of 4-ATP-[$BSANP_{PG}$] (Figure S4).

When the cells were incubated in the presence of NAC, the oxidative stress caused by NIR laser exposure with 4-ATP-[$BSANP_{PG}$] was lower than the NAC-free condition, as indicated by $I_{1142}$ /$I_{1077}$ (Figure 7C; $p < 0.05$). NAC was able to scavenge ROS species and reduce DMAB formation. Collectively, these experiments confirm that the cause for ROS generation was PTT with NIR laser exposure of 4-ATP-[$BSANP_{PG}$] and that the oxidative stress caused by PTT can be reduced using an antioxidant.

Intracellular ROS generation was further confirmed using a well-established fluorescence assay with the staining dye DCFDA.[62] ROS oxidize DCFDA to form the fluorescent molecule dichlorofluorescein (DCF). Basal level oxidative stress was observed without treatment and increased in the presence of 4-ATP-[$BSANP_{PG}$] (Figure 7C). A 2-fold increase in ROS was observed after 10 min of NIR laser exposure ($p < 0.01$), similar to the ROS levels detected by SERS based on $I_{1142}/I_{1077}$ under the same conditions (Figure 7C). A significant reduction in ROS was then observed ($p < 0.001$) with NAC present, with ROS values comparable to the no-treatment control condition. These obtained results with the DCFDA assay validate our observation using 4-ATP-[$BSANP_{PG}$] as a ROS detection probe with PTT.

## ■ CONCLUSIONS

In conclusion, we synthesized stable and biocompatible soft templated "raspberry gold nanostructures," 4-ATP-[$BSANP_{PG}$], with attractive physicochemical properties. In this strategy, polycation coated on protein nanoparticles (as a soft template) was used to facilitate gold shell formation, enriching gold anion on the cationic surface. The photothermal properties clearly indicate that 4-ATP-[$BSANP_{PG}$] could perform as an excellent hyperthermia agent for *in vitro* PTT under the irradiation of a 730 nm laser. Furthermore, our initial *in vitro* studies show that the nanostructures can be utilized for intracellular SERS imaging-guided efficient photothermal therapy using A549 human lung cancer cells as a


https://doi.org/10.1021/acsanm.2c02641
ACS Appl. Nano Mater. 2022, 5, 14356−14366

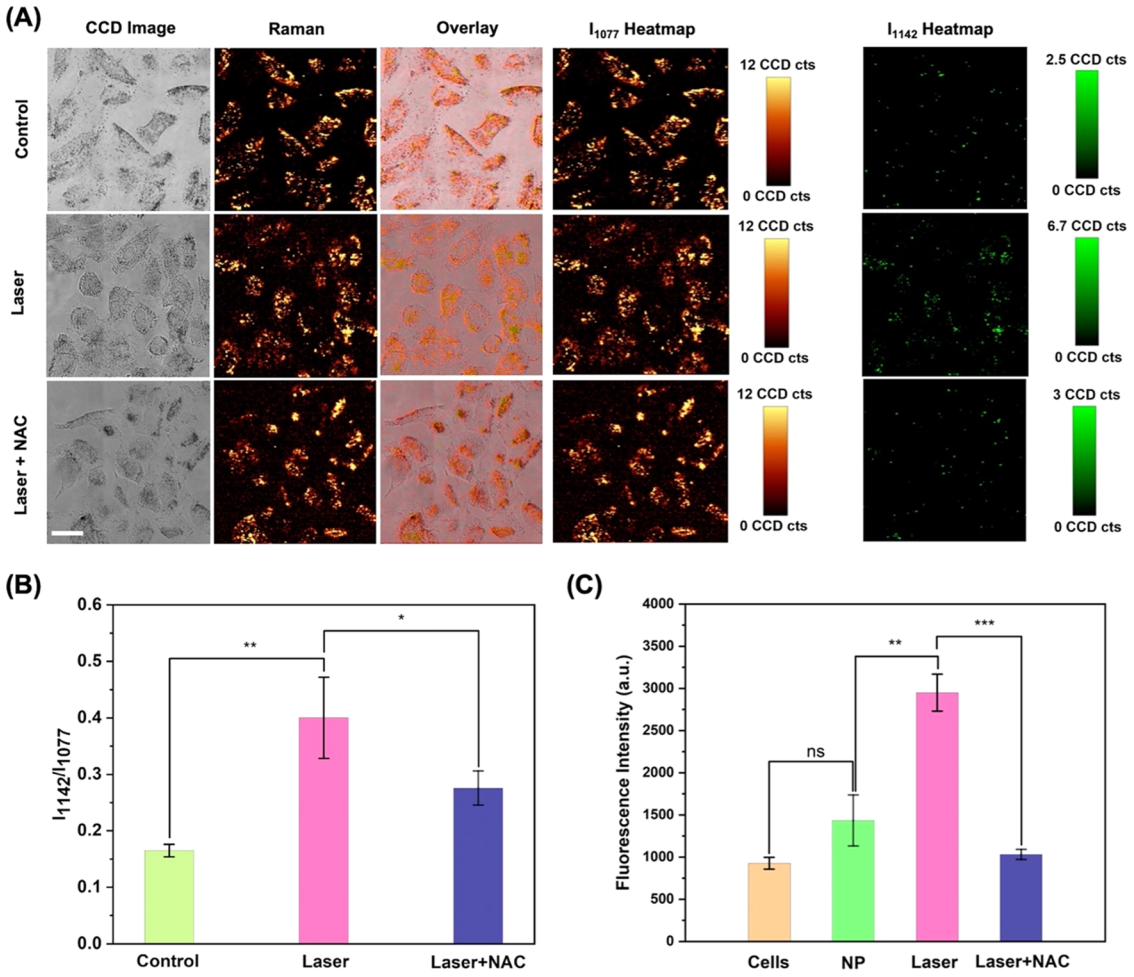


**Figure 7.** (A) Bright-field, Raman, and overlay images of A549 cells with 4-ATP-[$BSANP_{PG}$] (Control), with 4-ATP-[$BSANP_{PG}$] + NIR laser, and with 4-ATP-[$BSANP_{PG}$] + NIR laser + NAC (laser + NAC). SERS heat maps are shown for $I_{1077}$ $cm^{-1}$ (4-ATP) and $I_{1142}$ $cm^{-1}$ (DMAB). The scale bar is 20 $\mu$m. (B) Ratiometric detection of ROS based on $I_{1142}/I_{1077}$ for the three conditions examined. (C) DCFDA fluorescence assay for ROS detection. Fluorescence intensity is shown for untreated cells and cells exposed to 4-ATP-[$BSANP_{PG}$] (NP), 4-ATP-[$BSANP_{PG}$] + NIR laser, and 4-ATP-[$BSANP_{PG}$] + NIR laser + NAC (laser + NAC). Error bars represent the standard deviation $n = 3$, and statistical differences are provided at $p < 0.05$ (*) and $p < 0.01$ (**).

model. In addition, *in vitro* tracking of 4-ATP-[$BSANP_{PG}$] using SERS imaging provides a noninvasive tracking tool, which could be used to study particle uptake and their interaction with the ellular microenvironment. The reversible transformation of 4-ATP to DMAB (between oxidized and reduced states) makes it suitable to be used as a cellular oxidative stress indicator by measuring the SERS signals of 4-ATP-[$BSANP_{PG}$]. The ratiometric detection of ROS in response to therapeutics is promising toward feedback-assisted drug delivery, which could unlock a novel approach to monitor real-time therapeutic efficacy in response to therapeutics. Additional studies on dose-dependent ratiometric ROS detection are required to develop real-time ROS monitoring sensors. Furthermore, in the use of NIR light for *in vivo* applications, our core/shell "raspberry" nanostructures might find importance in light-controlled therapies.

## ■ ASSOCIATED CONTENT

### Supporting Information

The Supporting Information is available free of charge at https://pubs.acs.org/doi/10.1021/acsanm.2c02641.

Changes in SERS intensity for 4-ATP-[$BSANP_{PG}$] over five NIR heating cycles (Figures S1−S3) and additional details on the procedure for confocal Raman microscopy data acquisition and analysis (PDF)

## ■ AUTHOR INFORMATION


### Corresponding Author

**Geoffrey D. Bothun** − *Department of Chemical Engineering, University of Rhode Island, South Kingstown, Rhode Island 02881, United States;* orcid.org/0000-0002-7513-2417; Phone: +1-401-874-9518; Email: gbothun@uri.edu; Fax: +1-401-874-4689

### Authors

**Muzahidul I. Anik** − *Department of Chemical Engineering, University of Rhode Island, South Kingstown, Rhode Island 02881, United States;* orcid.org/0000-0002-5054-4175

**Animesh Pan** − *Department of Chemical Engineering, University of Rhode Island, South Kingstown, Rhode Island 02881, United States;* orcid.org/0000-0002-9222-687X

**Md Golam Jakaria** − *Department of Chemical Engineering, University of Rhode Island, South Kingstown, Rhode Island 02881, United States;* orcid.org/0000-0003-0584-6438




https://doi.org/10.1021/acsanm.2c02641
ACS Appl. Nano Mater. 2022, 5, 14356−14366

**Samantha A. Meenach** − *Department of Chemical Engineering, University of Rhode Island, South Kingstown, Rhode Island 02881, United States; Department of Biomedical and Pharmaceutical Science, University of Rhode Island, South Kingstown, Rhode Island 02881, United States;* orcid.org/0000-0002-3833-2110

Complete contact information is available at: https://pubs.acs.org/10.1021/acsanm.2c02641

### Author Contributions

[§]M.A. and A.P. contributed equally to this work.

### Notes

The authors declare no competing financial interest.

## ■ ACKNOWLEDGMENTS

Authors M.A., A.P., and G.B. were supported by the National Science Foundation Established Program to Stimulate Competitive Research (EPSCoR) under Cooperative Agreement OIA-1655221. Author Jakaria was supported by the Rhode Island Institutional Development Award (IDeA) Network of Biomedical Research Excellence from the National Institute of General Medical Sciences of the National Institutes of Health under Grant Number P20GM103430. Author Meenach was supported by the National Heart, Lung, and Blood Institute of the National Institutes of Health under Grant Number R01HL148727. The authors acknowledge Dr. Irene Andreu in the Rhode Island Consortium for Nanoscience and Nanotechnology for her microscopy support, Dr. Mitchel Gravely for his support with Raman microscopy and MATLAB coding, and Dr. Daniel Roxbury for the use of the NIR spectrometer.

## ■ REFERENCES

(1) Lv, Z.; He, S.; Wang, Y.; Zhu, X. Noble Metal Nanomaterials for NIR-Triggered Photothermal Therapy in Cancer. *Adv. Healthcare Mater.* **2021**, *10*, No. 202001806.

(2) Fernandes, N.; Rodrigues, C. F.; Moreira, A. F.; Correia, I. J. Overview of the Application of Inorganic Nanomaterials in Cancer Photothermal Therapy. *Biomater. Sci.* **2020**, *8*, 2990−3020.

(3) Nam, J.; Son, S.; Ochyl, L. J.; Kuai, R.; Schwendeman, A.; Moon, J. J. Chemo-Photothermal Therapy Combination Elicits Anti-Tumor Immunity against Advanced Metastatic Cancer. *Nat. Commun.* **2018**, *9*, No. 1074.

(4) Ma, Z.; Zhang, Y.; Zhang, J.; Zhang, W.; Foda, M. F.; Dai, X.; Han, H. Ultrasmall Peptide-Coated Platinum Nanoparticles for Precise NIR-II Photothermal Therapy by Mitochondrial Targeting. *ACS Appl. Mater. Interfaces* **2020**, *12*, 39434−39443.

(5) Dickerson, E. B.; Dreaden, E. C.; Huang, X.; El-Sayed, I. H.; Chu, H.; Pushpanketh, S.; McDonald, J. F.; El-Sayed, M. A. Gold Nanorod Assisted Near-Infrared Plasmonic Photothermal Therapy (PPTT) of Squamous Cell Carcinoma in Mice. *Cancer Lett.* **2008**, *269*, 57−66.

(6) Lin, Z.; Liu, Y.; Ma, X.; Hu, S.; Zhang, J.; Wu, Q.; Ye, W.; Zhu, S.; Yang, D.; Qu, D.; Jiang, J. Photothermal Ablation of Bone Metastasis of Breast Cancer Using PEGylated Multi-Walled Carbon Nanotubes. *Sci. Rep.* **2015**, *5*, No. 11709.

(7) Zhao, Y.; Zhao, T.; Cao, Y.; Sun, J.; Zhou, Q.; Chen, H.; Guo, S.; Wang, Y.; Zhen, Y.; Liang, X. J.; Zhang, S. Temperature-Sensitive Lipid-Coated Carbon Nanotubes for Synergistic Photothermal Therapy and Gene Therapy. *ACS Nano* **2021**, *15*, 6517−6529.

(8) Li, N.; Sun, Q.; Yu, Z.; Gao, X.; Pan, W.; Wan, X.; Tang, B. Nuclear-Targeted Photothermal Therapy Prevents Cancer Recurrence with Near-Infrared Triggered Copper Sulfide Nanoparticles. *ACS Nano* **2018**, *12*, 5197−5206.

(9) He, S.; Jiang, Y.; Li, J.; Pu, K. Semiconducting Polycomplex Nanoparticles for Photothermal Ferrotherapy of Cancer. *Angew. Chem., Int. Ed.* **2020**, *59*, 10633−10638.

(10) Liu, Y.; Wang, H.; Li, S.; Chen, C.; Xu, L.; Huang, P.; Liu, F.; Su, Y.; Qi, M.; Yu, C.; Zhou, Y. In Situ Supramolecular Polymerization-Enhanced Self-Assembly of Polymer Vesicles for Highly Efficient Photothermal Therapy. *Nat. Commun.* **2020**, *11*, No. 1724.

(11) Huang, X.; El-Sayed, M. A. Gold Nanoparticles: Optical Properties and Implementations in Cancer Diagnosis and Photothermal Therapy. *J. Adv. Res.* **2010**, *1*, 13−28.

(12) Li, X.; Hou, Y.; Meng, X.; Li, G.; Xu, F.; Teng, L.; Sun, F.; Li, Y. Folate Receptor-Targeting Mesoporous Silica-Coated Gold Nanorod Nanoparticles for the Synergistic Photothermal Therapy and Chemotherapy of Rheumatoid Arthritis. *RSC Adv.* **2021**, *11*, 3567−3574.

(13) Chen, X.; Zhang, Q.; Li, J.; Yang, M.; Zhao, N.; Xu, F.-J. Rattle-Structured Rough Nanocapsules with in-Situ-Formed Gold Nanorod Cores for Complementary Gene/Chemo/Photothermal Therapy. *ACS Nano* **2018**, *12*, 5646−5656.

(14) Jenkins, S. V.; Jung, S.; Shah, S.; Millett, P. C.; Dings, R. P. M.; Borrelli, M. J.; Griffin, R. J. Nanoscale Investigation and Control of Photothermal Action of Gold Nanostructure-Coated Surfaces. *J. Mater. Sci.* **2021**, *56*, 10249−10263.

(15) Hu, Y.; Huang, S.; Zhao, X.; Chang, L.; Ren, X.; Mei, X.; Chen, Z. Preparation of Photothermal Responsive and ROS Generative Gold Nanocages for Cancer Therapy. *Chem. Eng. J.* **2021**, *421*, No. 129744.

(16) Lee, S.-Y.; Shieh, M.-J. Platinum(II) Drug-Loaded Gold Nanoshells for Chemo-Photothermal Therapy in Colorectal Cancer. *ACS Appl. Mater. Interfaces* **2020**, *12*, 4254−4264.

(17) Emamzadeh, M.; Pasparakis, G. Polymer Coated Gold Nanoshells for Combinational Photochemotherapy of Pancreatic Cancer with Gemcitabine. *Sci. Rep.* **2021**, *11*, No. 9404.

(18) Wu, X.; Zhou, L.; Su, Y.; Dong, C. M. Plasmonic, Targeted, and Dual Drugs-Loaded Polypeptide Composite Nanoparticles for Synergistic Cocktail Chemotherapy with Photothermal Therapy. *Biomacromolecules* **2016**, *17*, 2489−2501.

(19) Du, C.; Zhou, L.; Qian, J.; He, M.; Dong, C. M.; Xia, J. D.; Zhang, Z. G.; Zhang, R. A Zwitterionic Polypeptide Nanocomposite with Unique NIR-I/II Photoacoustic Imaging for NIR-I/II Cancer Photothermal Therapy. *J. Mater. Chem. B* **2021**, *9*, 5484−5491.

(20) Tian, Y.; Zhang, Y.; Teng, Z.; Tian, W.; Luo, S.; Kong, X.; Su, X.; Tang, Y.; Wang, S.; Lu, G. PH-Dependent Transmembrane Activity of Peptide-Functionalized Gold Nanostars for Computed Tomography/Photoacoustic Imaging and Photothermal Therapy. *ACS Appl. Mater. Interfaces* **2017**, *9*, 2114−2122.

(21) Han, X.; Xu, Y.; Li, Y.; Zhao, X.; Zhang, Y.; Min, H.; Qi, Y.; Anderson, G. J.; You, L.; Zhao, Y.; Nie, G. An Extendable Star-Like Nanoplatform for Functional and Anatomical Imaging-Guided Photothermal Oncotherapy. *ACS Nano* **2019**, *13*, 4379−4391.

(22) Jia, Q.; Ge, J.; Liu, W.; Liu, S.; Niu, G.; Guo, L.; Zhang, H.; Wang, P. Gold Nanorod@silica-Carbon Dots as Multifunctional Phototheranostics for Fluorescence and Photoacoustic Imaging-Guided Synergistic Photodynamic/Photothermal Therapy. *Nanoscale* **2016**, *8*, 13067−13077.

(23) Wang, J.; Zhu, C.; Han, J.; Han, N.; Xi, J.; Fan, L.; Guo, R. Controllable Synthesis of Gold Nanorod/Conducting Polymer Core/Shell Hybrids Toward in Vitro and in Vivo near-Infrared Photothermal Therapy. *ACS Appl. Mater. Interfaces* **2018**, *10*, 12323−12330.

(24) Aioub, M.; Panikkanvalappil, S. R.; El-Sayed, M. A. Platinum-Coated Gold Nanorods: Efficient Reactive Oxygen Scavengers That Prevent Oxidative Damage toward Healthy, Untreated Cells during Plasmonic Photothermal Therapy. *ACS Nano* **2017**, *11*, 579−586.

(25) Lu, K. Y.; Jheng, P. R.; Lu, L. S.; Rethi, L.; Mi, F. L.; Chuang, E. Y. Enhanced Anticancer Effect of ROS-Boosted Photothermal Therapy by Using Fucoidan-Coated Polypyrrole Nanoparticles. *Int. J. Biol. Macromol.* **2021**, *166*, 98−107.

(26) Yang, B.; Chen, Y.; Shi, J. Reactive Oxygen Species (ROS)-Based Nanomedicine. *Chem. Rev.* **2019**, *119*, 4881−4985.
(27) Fan, J.; Ren, D.; Wang, J.; Liu, X.; Zhang, H.; Wu, M.; Yang, G. Bruceine D Induces Lung Cancer Cell Apoptosis and Autophagy via the ROS/MAPK Signaling Pathway in Vitro and in Vivo. *Cell Death Dis.* **2020**, *11*, No. 126.
(28) Luo, Y.; Ma, J.; Lu, W. The Significance of Mitochondrial Dysfunction in Cancer. *Int. J. Mol. Sci.* **2020**, *21*, No. 5598.
(29) Panieri, E.; Santoro, M. M. Ros Homeostasis and Metabolism: A Dangerous Liason in Cancer Cells. *Cell Death Dis.* **2016**, *7*, No. 2253.
(30) Manke, A.; Wang, L.; Rojanasakul, Y. Mechanisms of Nanoparticle-Induced Oxidative Stress and Toxicity. *Biomed Res. Int.* **2013**, *2013*, No. 942916.
(31) Chan, J.; Dodani, S. C.; Chang, C. J. Reaction-Based Small-Molecule Fluorescent Probes for Chemoselective Bioimaging. *Nat. Chem.* **2012**, *4*, 973−984.
(32) Klonis, N.; Rug, M.; Harper, I.; Wickham, M.; Cowman, A.; Tilley, L. Fluorescence Photobleaching Analysis for the Study of Cellular Dynamics. *Eur. Biophys. J.* **2002**, *31*, 36−51.
(33) Chen, L. Y.; Wang, C. W.; Yuan, Z.; Chang, H. T. Fluorescent Gold Nanoclusters: Recent Advances in Sensing and Imaging. *Anal. Chem.* **2015**, *87*, 216−229.
(34) Ramya, A. N.; Arya, J. S.; Madhukrishnan, M.; Shamjith, S.; Vidyalekshmi, M. S.; Maiti, K. K. Raman Imaging: An Impending Approach Towards Cancer Diagnosis. *Chem. - Asian J.* **2021**, *16*, 409−422.
(35) Giamougiannis, P.; Morais, C. L. M.; Grabowska, R.; Ashton, K. M.; Wood, N. J.; Martin-Hirsch, P. L.; Martin, F. L. A Comparative Analysis of Different Biofluids towards Ovarian Cancer Diagnosis Using Raman Microspectroscopy. *Anal. Bioanal. Chem.* **2021**, *413*, 911−922.
(36) Zhao, Z.; Chen, C.; Wei, S.; Xiong, H.; Hu, F.; Miao, Y.; Jin, T.; Min, W. Ultra-Bright Raman Dots for Multiplexed Optical Imaging. *Nat. Commun.* **2021**, *12*, No. 1305.
(37) Cui, K.; Fan, C.; Chen, G.; Qiu, Y.; Li, M.; Lin, M.; Wan, J. B.; Cai, C.; Xiao, Z. Para-Aminothiophenol Radical Reaction-Functionalized Gold Nanoprobe for One-to-All Detection of Five Reactive Oxygen Species in Vivo. *Anal. Chem.* **2018**, *90*, 12137−12144.
(38) Peng, R.; Si, Y.; Deng, T.; Zheng, J.; Li, J.; Yang, R.; Tan, W. A Novel SERS Nanoprobe for the Ratiometric Imaging of Hydrogen Peroxide in Living Cells. *Chem. Commun.* **2016**, *52*, 8553−8556.
(39) Nguyen, T. D.; Song, M. S.; Ly, N. H.; Lee, S. Y.; Joo, S. W. Nanostars on Nanopipette Tips: A Raman Probe for Quantifying Oxygen Levels in Hypoxic Single Cells and Tumours. *Angew. Chem.* **2019**, *131*, 2736−2740.
(40) Chen, J.; Wang, J.; Geng, Y.; Yue, J.; Shi, W.; Liang, C.; Xu, W.; Xu, S. Single-Cell Oxidative Stress Events Revealed by a Renewable SERS Nanotip. *ACS Sens.* **2021**, *6*, 1663−1670.
(41) Gu, X.; Wang, H.; Schultz, Z. D.; Camden, J. P. Sensing Glucose in Urine and Serum and Hydrogen Peroxide in Living Cells by Use of a Novel Boronate Nanoprobe Based on Surface-Enhanced Raman Spectroscopy. *Anal. Chem.* **2016**, *88*, 7191−7197.
(42) Popova, T. V.; Pyshnaya, I. A.; Zakharova, O. D.; Akulov, A. E.; Shevelev, O. B.; Poletaeva, J.; Zavjalov, E. L.; Silnikov, V. N.; Ryabchikova, E. I.; Godovikova, T. S. Rational design of albumin theranostic conjugates for gold nanoparticles anticancer drugs: Where the seed meets the soil? *Biomedicines* **2021**, *9*, No. 74.
(43) Wang, Q.; Guo, X.; Chen, Y.; Wu, Z.; Zhou, Y.; Sadaf, S.; Han, L.; Ding, X.; Sun, T. Theranostics System Caged in Human Serum Albumin as a Therapy for Breast Tumors. *J. Mater. Chem. B* **2020**, *8*, 6877−6885.
(44) Jeong, Y.; Jo, Y. K.; Kim, B. J.; Yang, B.; Joo, K., Il; Cha, H. J. Sprayable Adhesive Nanotherapeutics: Mussel-Protein-Based Nanoparticles for Highly Efficient Locoregional Cancer Therapy. *ACS Nano* **2018**, *12*, 8909−8919.
(45) Chen, J.; Chen, Q.; Liang, C.; Yang, Z.; Zhang, L.; Yi, X.; Dong, Z.; Chao, Y.; Chen, Y.; Liu, Z. Albumin-Templated Biomineralizing Growth of Composite Nanoparticles as Smart Nano-Theranostics for Enhanced Radiotherapy of Tumors. *Nanoscale* **2017**, *9*, 14826−14835.
(46) Karthikeyan, S.; Bharanidharan, G.; Ragavan, S.; Kandasamy, S.; Chinnathambi, S.; Udayakumar, K.; Mangaiyarkarasi, R.; Suganya, R.; Aruna, P.; Ganesan, S. Exploring the Binding Interaction Mechanism of Taxol in β-Tubulin and Bovine Serum Albumin: A Biophysical Approach. *Mol. Pharmaceutics* **2019**, *16*, 669−681.
(47) Pan, A.; Jakaria, M. G.; Meenach, S. A.; Bothun, G. D. Radiofrequency and Near-Infrared Responsive Core−Shell Nanostructures Using Layersome Templates for Cancer Treatment. *ACS Appl. Bio Mater.* **2020**, *3*, 273−281.
(48) Chen, Q.; Xu, L.; Liang, C.; Wang, C.; Peng, R.; Liu, Z. Photothermal Therapy with Immune-Adjuvant Nanoparticles Together with Checkpoint Blockade for Effective Cancer Immunotherapy. *Nat. Commun.* **2016**, *7*, No. 10304.
(49) Schneider, C. A.; Rasband, W. S.; Eliceiri, K. W. NIH Image to ImageJ: 25 Years of Image Analysis. *Nat. Methods* **2012**, *9*, 671−675.
(50) Luebbert, C. C. E.; Mansa, R.; Rahman, R.; Jakubek, Z. J.; Frahm, G. E.; Zou, S.; Johnston, M. J. W. Influence of Bound Dodecanoic Acid on the Reconstitution of Albumin Nanoparticles from a Lyophilized State. *Sci. Rep.* **2021**, *11*, No. 4768.
(51) Khramtsov, P.; Kalashnikova, T.; Bochkova, M.; Kropaneva, M.; Timganova, V.; Zamorina, S.; Rayev, M. Measuring the Concentration of Protein Nanoparticles Synthesized by Desolvation Method: Comparison of Bradford Assay, BCA Assay, Hydrolysis/UV Spectroscopy and Gravimetric Analysis. *Int. J. Pharm.* **2021**, *599*, No. 120422.
(52) Weber, C.; Coester, C.; Kreuter, J.; Langer, K. Desolvation Process and Surface Characterisation of Protein Nanoparticles. *Int. J. Pharm.* **2000**, *194*, 91−102.
(53) Abolhassani, H.; Shojaosadati, S. A. A Comparative and Systematic Approach to Desolvation and Self-Assembly Methods for Synthesis of Piperine-Loaded Human Serum Albumin Nanoparticles. *Colloids Surf., B* **2019**, *184*, No. 110534.
(54) Liebig, F.; Sarhan, R. M.; Schmitt, C. N. Z. Z.; Thünemann, A. F.; Prietzel, C.; Bargheer, M.; Koetz, J. Gold Nanotriangles with Crumble Topping and Their Influence on Catalysis and Surface-Enhanced Raman Spectroscopy. *ChemPlusChem* **2020**, *85*, 519−526.
(55) Wang, T.; Zhang, Z.; Liao, F.; Cai, Q.; Li, Y.; Lee, S.-T.; Shao, M. The Effect of Dielectric Constants on Noble Metal/Semiconductor SERS Enhancement: FDTD Simulation and Experiment Validation of Ag/Ge and Ag/Si Substrates. *Sci. Rep.* **2014**, *4*, No. 4052.
(56) Rezvanian, A.; Beigzadeh, B.; Davaei Markazi, A. H.; Halabian, M. Feedback Control of Temperature in Specific Geometry of Porous Media: Application to Hyperthermia. *J. Therm. Anal. Calorim.* **2020**, *141*, 1559−1568.
(57) Zeng, J.; Goldfeld, D.; Xia, Y. A Plasmon-Assisted Optofluidic System for Measuring the Photothermal Conversion Efficiencies of Gold Nanostructures and Controlling an Electrical Switch. *Angew. Chem. Int. Ed.* **2013**, *52*, 4169−4173.
(58) Jiang, T.; Song, J.; Zhang, W.; Wang, H.; Li, X.; Xia, R.; Zhu, L.; Xu, X. Au−Ag@Au Hollow Nanostructure with Enhanced Chemical Stability and Improved Photothermal Transduction Efficiency for Cancer Treatment. *ACS Appl. Mater. Interfaces* **2015**, *7*, 21985−21994.
(59) Zong, S.; Wang, Z.; Yang, J.; Cui, Y. Intracellular PH Sensing Using P-Aminothiophenol Functionalized Gold Nanorods with Low Cytotoxicity. *Anal. Chem.* **2011**, *83*, 4178−4183.
(60) Florence, T. M. The Production of Hydroxyl Radical from Hydrogen Peroxide. *J. Inorg. Biochem.* **1984**, *22*, 221−230.
(61) Lin, L. K.; Stanciu, L. A.; Bisphenol, A. Detection Using Gold Nanostars in a SERS Improved Lateral Flow Immunochromatographic Assay. *Sen. Actuators, B* **2018**, *276*, 222−229.
(62) Duanghathaipornsuk, S.; Farrell, E. J.; Alba-Rubio, A. C.; Zelenay, P.; Kim, D.-S. Detection technologies for reactive oxygen species: fluorescence and electrochemical methods and their applications. *Biosensors* **2021**, *11*, No. 30.


https://doi.org/10.1021/acsanm.2c02641
*ACS Appl. Nano Mater.* 2022, 5, 14356−14366